

Hard X-ray photoemission spectroscopy of LaVO₃/SrTiO₃: Band alignment and electronic reconstruction

M. Stübinger,¹ J. Gabel,^{1,2} P. Scheiderer,¹ M. Zapf,¹ M. Schmitt,¹ P. Schütz,¹ B. Leikert,¹ J. Küspert,¹ M. Kamp,¹ P.K. Thakur,² T.-L. Lee,² P. Potapov,³ A. Lubk,³ B. Büchner,³ M. Sing,¹ and R. Claessen¹

¹Physikalisches Institut and Würzburg-Dresden Cluster of Excellence *ct.qmat*,
Universität Würzburg, Am Hubland, 97074 Würzburg, Germany

²Diamond Light Source Ltd., Didcot, Oxfordshire OX11 0DE, United Kingdom

³Leibniz Institute for Solid State and Materials Research and
Würzburg-Dresden Cluster of Excellence *ct.qmat*, 01069 Dresden, Germany

(Dated: May 27, 2021)

The heterostructure consisting of the Mott insulator LaVO₃ and the band insulator SrTiO₃ is considered a promising candidate for future photovoltaic applications. Not only does the (direct) excitation gap of LaVO₃ match well the solar spectrum, but its correlated nature and predicted built-in potential, owing to the non-polar/polar interface when integrated with SrTiO₃, also offer remarkable advantages over conventional solar cells. However, experimental data beyond the observation of a thickness-dependent metal-insulator transition is scarce and a profound, microscopic understanding of the electronic properties is still lacking. By means of soft and hard X-ray photoemission spectroscopy as well as resistivity and Hall effect measurements we study the electrical properties, band bending, and band alignment of LaVO₃/SrTiO₃ heterostructures. We find a critical LaVO₃ thickness of five unit cells, confinement of the conducting electrons to exclusively Ti 3d states at the interface, and a potential gradient in the film. From these findings we conclude on electronic reconstruction as the driving mechanism for the formation of the metallic interface in LaVO₃/SrTiO₃.

I. INTRODUCTION

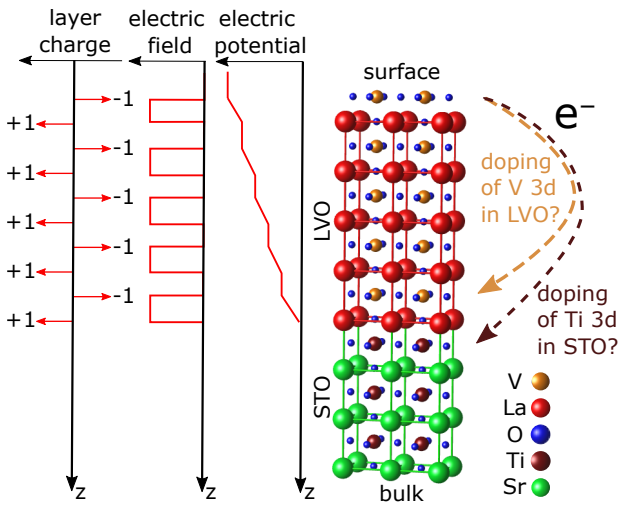


FIG. 1. In the electronic reconstruction model the polar discontinuity at the interface of the LVO/STO heterostructure leads to a potential built-up in LVO. It can be compensated by transferring electrons from the surface to the interface. In LVO/STO, the 3d shells of both Ti as well as V could host the electrons.

Transition-metal oxides with strong electronic correlations are of great interest in condensed-matter physics due to their vast amount of unique properties. Among them are high-temperature superconductivity, colossal magnetoresistance, and metal-to-insulator transitions, functionalities, that offer a versatile platform to build

on future devices [1–6]. Specifically, the strong Coulomb repulsion of the rather localized valence electrons in transition-metal oxides with incomplete valence shells can lead to a Mott insulating ground state [7]. Mott insulators with a charge gap in the regime of visible light have been proposed to be promising candidates for photovoltaic applications due to their favorable absorption properties regarding the solar spectrum [8, 9]. Furthermore, Mott insulators as photovoltaic materials have some intriguing advantages over conventional semiconductors. By so called impact ionization more than one electron per incoming photon can be excited before thermalization. This is due to electron-electron interactions being much faster than electron-phonon interactions, which are the dominant mechanism for thermalization in conventional semiconductors [10, 11]. Besides, a fast separation of photogenerated electron-hole pairs may be achieved by the antiferromagnetic background of many Mott insulators, which acts as an energy buffer for photoexcited carriers on femtosecond time scales [12].

The system to be studied here, LaVO₃ (LVO), is such an antiferromagnetic Mott insulator with an optical gap of 1.1 eV [13, 14]. Its usage for photovoltaic applications can be further optimized by integrating this material as thin film with the band insulator SrTiO₃ (STO) as substrate into a heterostructure, since the polar discontinuity at the interface may lead to a potential gradient in the LVO film, which would help to separate the photogenerated electron hole-pairs. While—in the ionic limit—STO consists of charge-neutral layers along the [001] direction, LVO is built up by alternating positive (LaO)⁺ and negative (VO₂)⁻ layers. The polar discontinuity between STO and LVO induces an electrostatic

potential which diverges with LVO film thickness (see Fig. 1). Above a critical film thickness, the interface turns conductive [15]. Density-functional theory (DFT) calculations [8] show that in such a situation the internal potential gradient in the LVO/STO heterostructure persists and can be exploited to separate photogenerated electron-hole pairs. This and the metallic interface and surface serving as electrodes to extract the charge carriers, renders LVO/STO an interesting candidate for oxide-based solar cells [8, 9, 13, 16, 17].

Up to now, an in-depth understanding of this heterostructure regarding the emerging metallicity and the role of the internal potential is still lacking. For future device applications in photovoltaics, however, it is of great importance to comprehend the complete electronic band diagram and the role of charges in this system to tailor the desired properties. In our study, we investigate the charge transfer and the electronic band alignment in LVO/STO by transport measurements and photoemission spectroscopy. We show that conductivity is not induced by oxygen vacancies in the substrate but due to electronic reconstruction. The STO Ti $3d$ bands host the electrons giving rise to the metallicity while there is no sign for metallic V $3d$ states at the Fermi energy.

II. EXPERIMENTAL DETAILS

To prepare STO substrates with TiO_2 termination, the substrates were rinsed in deionized water, etched with hydrofluoric acid and subsequently annealed in oxygen [18]. The LVO thin films were grown by pulsed laser deposition at a substrate temperature of 550°C and an oxygen pressure of 10^{-6} mbar. The LVO was ablated from a polycrystalline LaVO_4 target. The pulsed KrF excimer laser was set to a repetition rate of 1 Hz and a laser fluency of 1.5 J/cm^2 . Reflection high-energy electron diffraction (RHEED) was employed to monitor the film growth in real time.

Atomic resolution scanning transmission electron microscopy (STEM) of the interface was performed in a probe-corrected FEI Titan³ microscope equipped with a Gatan Tridiem energy filter and operating at 300kV acceleration voltage.

Photoemission spectroscopy experiments were performed at the beamline I09 at Diamond Light Source. Soft x-rays with the photon energy set to $h\nu = 460.05$ eV and 517.7 eV were used for measurements at the Ti L and V L resonance, respectively, and a sample temperature of 60 K. Additionally, hard X-ray photoemission spectroscopy (HAXPES) with a photon energy of 3 keV was used at room temperature. The EW4000 photoelectron analyzer (VG Scienta, Sweden) was equipped with a wide-angle acceptance lens. To prevent overoxidation of the LVO films, a portable ultrahigh vacuum (UHV) suitcase with a base pressure in the 10^{-9} mbar range was used to ship the samples to Diamond.

Temperature-dependent transport measurements were

performed with a Physical Property Measurement System (Quantum Design, USA). The samples were electrically contacted by ultrasonic bonding with Al wires arranged in van der Pauw geometry.

III. CHARACTERIZATION OF STRUCTURAL, CHEMICAL AND ELECTRONIC PROPERTIES

Figure 2 shows the growth characterization of the LVO films. Figure 2(a) displays the intensity modulations of the specular RHEED beam (see red circles in inset) during the film growth. The regular intensity oscillations signal layer-by-layer growth, while the RHEED pattern at the end of the growth confirms an atomically smooth film surface. In Fig. 2(b) the X-ray diffraction (XRD) pattern of a sample with a 50 unit cells (uc) thick LVO film exhibits peaks corresponding only to a (pseudo)cubic (001) LVO film as well as substrate peaks, demonstrating the phase purity of the sample. The atomic force microscopy (AFM) image in Fig. 2(c) reveals the surface topography of a 10 uc LVO/STO sample. One recognizes the terraced structure reflecting the miscut STO substrate whose surface is covered by a smooth film of uniform thickness. Also shown is a height profile along the red line indicated in the AFM image. Figure 2(d, top) shows the interface of a 30 uc LVO/STO sample obtained in high-angle annular dark field (HAADF) STEM mode (contrast of atomic columns roughly proportional to squared atomic number) with the layer sequence matching exactly the schematic sequence in Fig. 1. Figure 2(d, bottom) displays chemical maps of the same region for substrate and film elements from STEM-EELS. The observable slight signal intermixing such as Ti traces at the adjacent La and V layers or La traces at the adjacent Ti and Sr layers is mainly caused by electron beam spreading within the sample due to scattering delocalization. Therefore, within the precision of the STEM technique, there were no hints for an off-stoichiometry or intermixing, and the LVO/STO interface was found structurally and chemically well defined on an atomic level.

After having confirmed the structural and chemical quality of the grown films, we now investigate the transport properties with resistivity and Hall effect measurements. Although both components are insulators, the LVO/STO heterostructure can become conductive as depicted in the model of intrinsic electronic reconstruction in Fig. 1: According to this model, the built-in potential can be compensated by transferring half an electron per two-dimensional unit cell from the surface to the interface where transition metal $3d$ orbitals can host the electrons, resulting in a metallic interface. This mechanism has been well investigated for the related LAO (LaAlO_3)/STO system [19–21]. Previous DFT calculations as well as hard X-ray core-level photoemission spectroscopy of trilayer LAO/LVO/LAO grown on STO suggest that charge transfer may involve not only Ti but also V sites and the involvement of the latter may lead

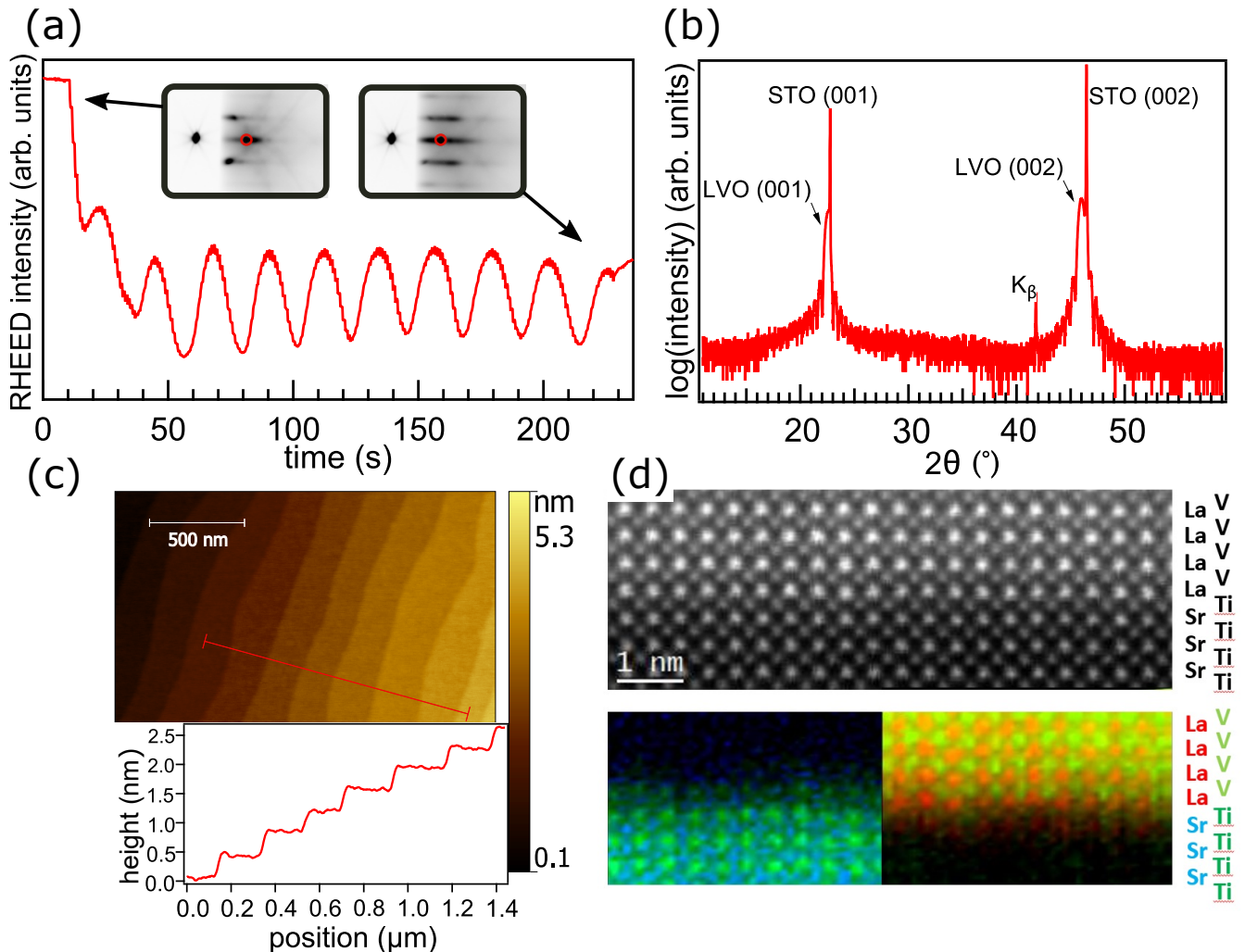


FIG. 2. (a) Monitoring of film growth by RHEED. Regular intensity oscillations of the specular reflex indicate layer-by-layer growth. The RHEED patterns confirm that the substrate and the film surface after the growth of LVO are atomically smooth. (b) X-ray diffractogram of a phase pure 50 uc LVO film on STO. (c) AFM image of a 10 uc LVO/STO sample along with a height profile signaling good quality of the sample surface. (d) Scanning transmission electron microscopy of a 30 uc LVO/STO sample. (top) HAADF-STEM image showing the interface structure. (bottom) Chemical maps of the same region for substrate and film elements from STEM-EELS. The images confirm a chemically sharp interface and a good structural film quality.

to the emergence of strong electron correlations [8, 22]. Hence, for device applications, it is crucial to elucidate where exactly the transferred electrons reside: the Ti $3d$ states of the STO substrate, resulting in a slightly n -doped semiconducting interface layer, or the V $3d$ states via self-doping within the LVO film, inducing a band-filling controlled Mott-insulator-to-metal transition and hence a correlated metal at the interface. However, one should keep in mind that the electronic reconstruction model in its ideal form is still highly disputed and that additional, extrinsic mechanisms for the generation of the two-dimensional electron system (2DES) like interfacial intermixing [23, 24], oxygen vacancies [25, 26] or surface adsorbates [27–29] might be at work.

Figure 3 (a) shows the room temperature sheet conductance of LVO/STO samples with different film thick-

nesses. The insulator-to-metal transition occurs at a film thickness of 5 uc. Films thinner (thicker) than 5 uc are insulating (conductive). A more intricate situation is found for the transition at 5 uc, where we fabricated and measured four samples in total. Two of the samples are metallic with a sheet conductance of the order of $10^{-5}/\text{Ohm}$, which is comparable with the thicker samples. The other two are insulating just like the films with a lower thickness. This behavior suggests that at the critical thickness the sample’s metallicity can be sensitive to small variations in the substrate and film quality.

Our result of an insulator-to-metal transition at a film thickness of 5 uc is consistent with the findings by Hotta *et al.*, who reported a transition between 4 and 5 uc [15]. In a recent study, Hu *et al.* pointed out that the mechanism behind the conductivity strongly depends on the

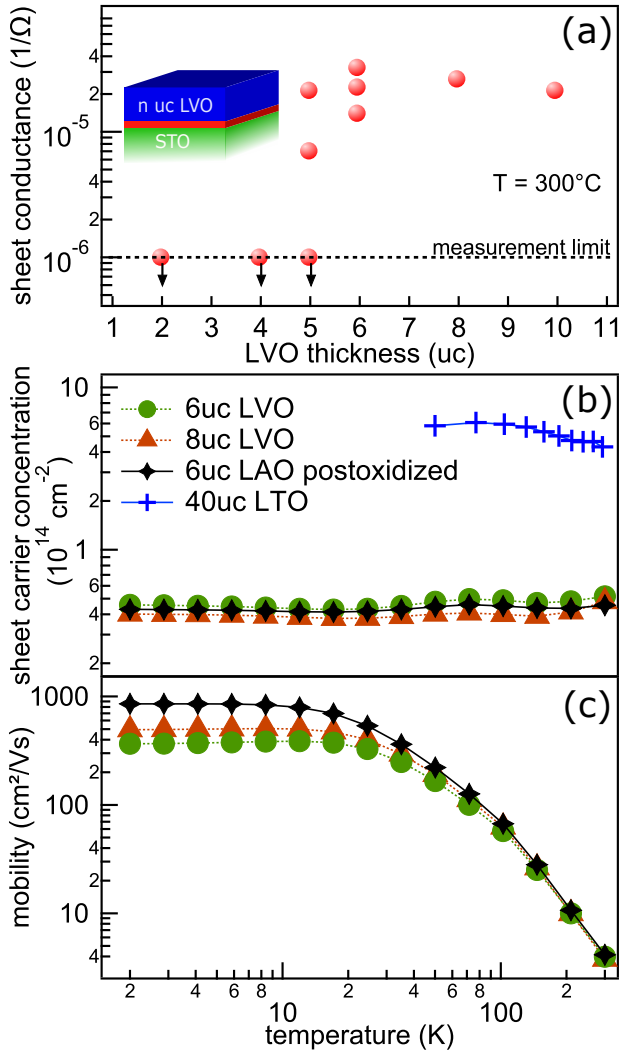


FIG. 3. (a) Sheet conductance of the LVO/STO heterostructure at room temperature for varying film thickness. Samples with LVO thicknesses above the critical value of five unit cells show metallic behavior. (b) Sheet carrier concentrations of metallic LVO/STO as well as LAO/STO samples and of the doped Mott insulator LTO. The behavior of the LVO films resembles that of post-oxidized LAO/STO. (c) Mobilities of metallic LVO/STO as well as LAO/STO samples.

growth parameters, especially the growth rate and the substrate temperature [30]. Authors who used a higher substrate temperature (up to 750°C) reported oxygen-vacancy-induced conductivity [31]. This is mainly due to oxygen vacancies in STO that act as electron donors, rendering the substrate metallic [32]. Such metallicity solely based on STO is well established in literature [33–40]. Other groups used a lower substrate temperature (around 600°C) and attributed the observed conductivity to the intrinsic mechanism of electronic reconstruction [15, 41]. Therefore, to suppress charges donated by oxygen vacancies in the substrate it is critical to cautiously adjust the growth parameters. Note that post-annealing in high oxygen pressures to get rid of oxygen vacancies is not pos-

sible as the thermodynamically more stable LaVO₄ phase would quickly form. We rather used a particularly low substrate temperature of 550°C to minimize the creation of oxygen vacancies.

Figure 3 (b) depicts the temperature-dependent sheet carrier concentrations for different oxide heterostructures. The carrier concentrations of the metallic LVO/STO samples are essentially constant over the whole temperature range with a value of about $5 \cdot 10^{13} \text{ cm}^{-2}$. This value is orders of magnitude lower than those for samples loaded with oxygen vacancies [30]. It is comparable to the values reported for intrinsic transport behavior [15, 30, 41] but much lower than the theoretical value of $3.28 \cdot 10^{14} \text{ cm}^{-2}$ that is expected when half an electron per unit cell is transferred to the interface in the ideal electronic reconstruction scenario. One also should note that variations of the cation stoichiometry likewise may play a decisive role in the transport properties. In a recent study of 50 uc thick LVO films grown on STO, it has been found that a slight La-deficiency is mandatory for a metallic interface [42].

Interestingly, the temperature-dependent carrier concentrations [Fig. 3 (b)] and mobilities [Fig. 3 (c)] of the metallic LVO/STO samples are almost identical to those of a post-annealed LAO/STO sample, whose transport properties have been shown to result from an intrinsic mechanism [43]. These observations suggest that conductivity in the LVO/STO samples is not induced by oxygen vacancies in the substrate but is of intrinsic origin. Furthermore, the type of mobile carriers seems to be the same as in LAO/STO samples, i.e., electrons in Ti 3*d* bands of STO (rather than electrons in V 3*d* bands of LVO) are responsible for the conductivity. Indeed, electron doping of STO by an intrinsic electronic reconstruction type of mechanism creates a 2DES with a small density of charge carriers that are hosted by an almost empty Ti 3*d* shell corresponding to a $d^{0+\delta}$ configuration. On the contrary, electron doping of V 3*d* states in LVO would result in a slightly doped Mott insulator with a $d^{2+\delta}$ occupancy. Such a Mott insulator, slightly *n*-doped into the metallic regime, would have a much higher charge carrier density since it is close to half band-filling. To compare our results for LVO/STO with those of a doped Mott insulator, Fig. 3 (b) also depicts the carrier concentration of a 40 uc thick LaTiO₃ (LTO) film which is *p*-doped by excess oxygen just into the metallic regime [6]. For this doped Mott insulator we measure a much higher carrier concentration than for LVO/STO. Thus, with the charge carrier concentration of LVO/STO being almost identical to that of LAO/STO but way smaller than that for doped LTO we conclude that the metallicity of our LVO/STO samples is solely based on Ti 3*d* states of the STO substrate.

To reveal the elemental and orbital character of the charge carriers, being responsible for the conductivity in this system, we employed resonant photoemission spectroscopy (ResPES) in the soft x-ray regime. In the case of LAO/STO, it is well established that the Ti 3*d* charge

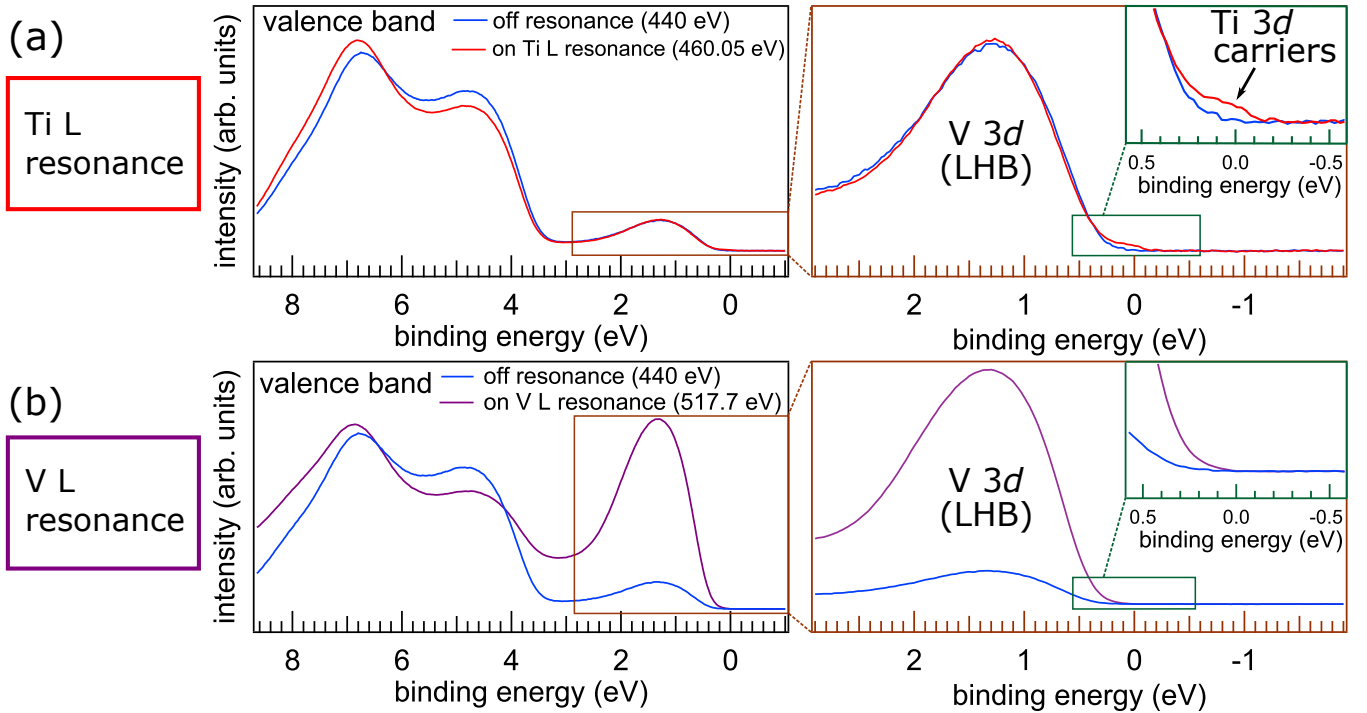


FIG. 4. (a) ResPES at the Ti L edge of a 5 uc LVO film on STO. On resonance, there is spectral weight at the Fermi energy, indicating metallic Ti $3d$ charge carriers (marked by arrow). (b) ResPES at the V L edge of the same sample. On resonance, the lower Hubbard band (marked as V $3d$ LHB) below the Fermi energy strongly resonates but there is no spectral weight at the Fermi energy to be seen, indicating the absence of metallic V $3d$ charge carriers.

carriers at E_F , forming the buried 2DES, can be studied by this technique despite the small carrier concentrations [43–45]. Accordingly, we measured the valence band spectra of a 5 uc LVO/STO sample with a conducting interface, both at the Ti L and V L edges. The sample was aligned parallel to the Γ - X direction. The spectra were integrated over an angular range of $\pm 23^\circ$ around normal emission (NE) parallel to the analyzer slit and $\pm 0.15^\circ$ perpendicular to the analyzer slit.

Figure 4 (a) shows the valence band spectrum recorded on the Ti L resonance together with an off-resonance spectrum. On resonance, there is spectral weight discernible at the Fermi energy. This is a clear indication of Ti $3d$ charge carriers, corroborating our reasoning from the transport data.

Figure 4 (b) depicts the V resonance for the same sample. Here, the spectral weight related to the lower Hubbard band (LHB) at around 1.5 eV below the Fermi energy strongly resonates when the photon energy is tuned to the V L resonance. In contrast to the Ti L resonance, however, no spectral weight is seen at the Fermi energy, indicating the absence of metallic V $3d$ charge carriers. Again, we arrive at the conclusion that the conductivity in LVO/STO is solely related to Ti $3d$ charge carriers.

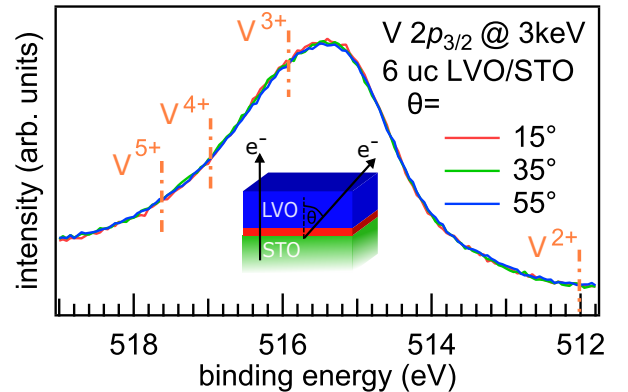


FIG. 5. V $2p_{3/2}$ photoemission spectra of a 6 uc LVO/STO sample for different electron emission angles. The spectra measured with higher angles off normal emission are more surface sensitive. The fact that there is no significant angle-dependence suggests a homogeneous distribution of vanadium with a uniform valence over the whole film and accordingly the absence of electron doping into V $3d$ states.

IV. CHEMICAL AND BAND STRUCTURE INFORMATION FROM HAXPES

To corroborate the results of our transport and ResPES data and to get the full band picture of the LVO/STO heterostructure, we investigated the electronic

structure by HAXPES.

A. Homogeneous valence distribution and potential gradient in the LaVO_3 film from core-level analysis

As Wadati *et al.* pointed out, LVO is not stable in air since the surface will oxidize, leading to a $V 2p$ photoemission spectrum with spectral weight shifted towards higher binding energies, reflecting a change from the nominal V^{3+} valence of stoichiometric LVO to a higher V valence [46]. This is possible because the transition metal vanadium possesses oxidation states ranging from 0 to 5+. Vanadium oxides in general—when exposed to air—tend to further oxidize at their surface, in this case to V^{4+} and V^{5+} [47]. For these reasons, we used a UHV suitcase for shipping the samples from the PLD chamber to the synchrotron to preserve the stoichiometric LVO with its intrinsic electronic structure.

Figure 5 depicts the $V 2p_{3/2}$ core level spectra of a 6 uc LVO/STO sample at 3 keV photon energy collected at different electron emission angles θ . In comparison to reported binding energies for different V valences, the spectrum appears most closely attributable to the V^{3+} oxidation state [47]. The broadening is mainly due to the partially filled d -shell in LVO. The two V $3d$ electrons couple to the core hole, leading to a multiplet splitting of the photoemission line [48].

The spectra for different emission angles, i.e., recorded with different probing depths, are essentially identical, meaning that the distribution of V valence states is homogeneous throughout the film.

To gain insight into a possible electronic potential building up across the film, we measured three different LVO/STO samples with varying LVO thickness (3 uc, 6 uc and 9 uc). For all film core-levels we notice a similar trend. With increasing film thickness, there is an increasing energy shift towards lower binding energies. Exemplarily, we show angle-integrated La $4d$ core-level spectra in Fig. 6 (top). As can be clearly seen, the shift between the spectra of the 3 uc and the 6 uc films is bigger than that between the spectra of the 6 uc and 9 uc films. Note that these spectral shifts are a property of the LVO films as no shifts are seen in the substrate core-level spectra (not shown here). Such a monotonic shift of film core-level spectra with thickness can be a signature of a built-in potential, as has been reported, e.g., for LaCrO_3 and LaFeO_3 films grown on STO [49, 50]. In contrast, in a HAXPES study of LAO/STO, the film core level spectra did not shift with film thickness, indicating that there is no sizable potential gradient in this system [51].

To verify that there is indeed a built-in potential in the LVO film, we compare in Fig. 6 (middle) the La $4d$ spectrum of a 6 uc LVO film with that of a 30 uc thick reference sample. This reference should approximately have no potential gradient, which can be understood in an ideal electronic reconstruction picture: When assum-

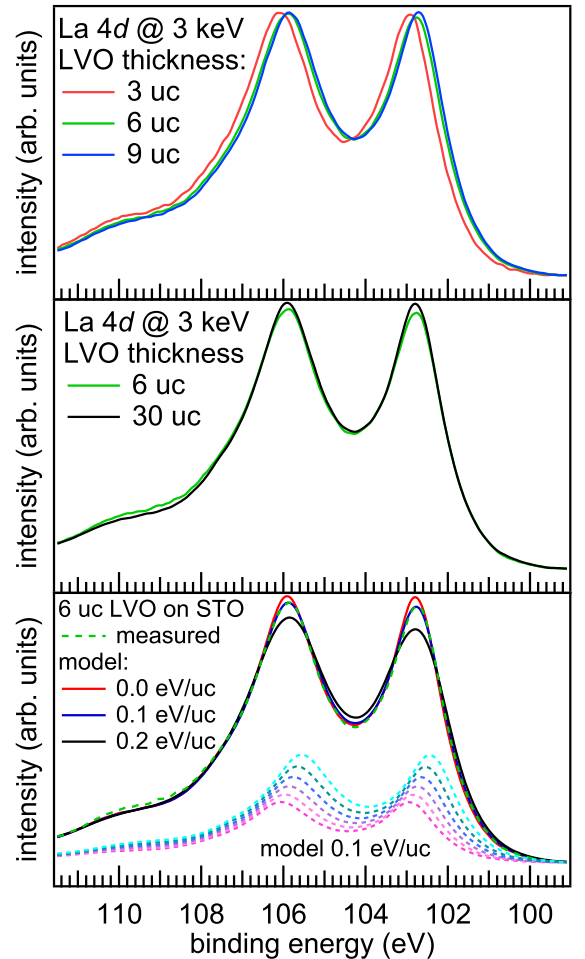


FIG. 6. (top) Angle-integrated La $4d$ spectra for three different LVO/STO samples with LVO film thicknesses of 3, 6 and 9 uc integrated over an emission angle θ of $(35 \pm 28)^\circ$. One can see an energy shift towards lower binding energies with increasing film thickness. (middle) Comparison of the La $4d$ spectrum of the film with a thickness of 6 uc with a reference spectrum of a 30 uc thick film. The former is broader consistent with a potential gradient in the film. (bottom) Comparison of the spectrum of the 6 uc LVO/STO sample with model spectra for three different potential gradients. The model spectrum based on a uniform gradient of 0.1 eV/uc best matches the measured spectrum. Also shown is the decomposition of the model spectrum into its single components, corresponding to the six layers. Each single spectrum is exponentially damped according to the depth of its corresponding layer with its energy shift being determined by the gradient.

ing the highest occupied LVO band to cross the Fermi energy at a thickness of 30 uc instead of 6 uc, the (average) potential gradient is a factor of five smaller. Indeed, the spectrum of the 6 uc film is slightly broader than that of the thick one, which is consistent with a potential gradient in thinner films.

To obtain a rough estimate of the gradient, we simulate the measured La $4d$ spectrum by the superposition of six La $4d$ reference spectra measured from the 30 uc

sample, one for each of the six film layers. Each reference spectrum is shifted in energy according to the potential gradient. The intensity I from each layer n is assumed to be damped according to

$$I(z = na) = I_0 \exp(-na/\lambda \cos \theta), \quad (1)$$

where I_0 is the undamped signal, λ the inelastic mean free path of the photoelectrons, θ the electron emission angle, z the depth and a the lattice constant of the film. The comparison between the measured 6 uc spectrum and model spectra for three different gradients is depicted in Fig. 6 (bottom). With such a coarse model, there is already a good match between the data and the simulated spectrum for a slope of 0.1 eV/uc, whereas the other model spectra deviate more strongly from the measured spectrum, particularly near the peak maxima.

To refine our quantitative analysis of the potential gradient further, we *fit* the measured La 4d and V 2p_{3/2} spectra at once for each of the three film thicknesses. The results are depicted in the top panels of Fig. 7 (a). As before, each measured core-level spectrum is built up from the spectra of the individual film layers. In contrast to before, the energy shifts across the film are no longer fixed but are fitted. The energy positions of the reference spectra are the only fitting parameters. The layer resolved spectra obtained from the best fits for all three samples are shown in the bottom panels of Fig. 7 (a). Altogether, one can see that the broadening and the thickness-dependent energy shifts of the measured film core-levels can be well reproduced by the fits with a significant potential gradient at work. From the energy shifts of the layer-resolved spectra for both La 4d and V 2p, we can deduce the potential profiles in the films, which are depicted in Fig. 7 (b). Here, the energy shifts of the individual spectra for all film layers are plotted relative to the spectrum of the first layer above the interface of the 6 uc sample, with a positive energy shift indicating a shift to a lower binding energy. We obtain a potential gradient of around 0.1 eV/uc for the 3 uc and 6 uc films, while for the 9 uc film the potential profile appears to level off toward the surface, resulting in a slightly lower average gradient. Furthermore, there is no significant potential offset between the three samples right at the interface.

In summary, we indeed find a sizable potential gradient, but it is significantly lower than the theoretical value of around 0.3 eV/uc [8]. One possible reason for this could lie in charged interface or surface defects or structural distortions, which partially screen out the gradient and have not been considered in the theoretical calculations [8].

B. Band bending in the SrTiO₃ substrate from core-level analysis

Due to the enhanced probing depth of HAXPES, one can study not only the film but also the substrate core-

levels. Figure 8 depicts the Ti 2p_{3/2} and the Sr 3d spectra of a 6 uc LVO/STO sample recorded at 3 keV photon energy for different electron emission angles θ .

Turning first to the Ti 2p_{3/2} spectra in Fig. 8, the corresponding Ti oxidation state is, by comparing with the reference spectrum of Nb-doped STO, readily identified as 4+. More interestingly, this comparison reveals additional spectral weight at low binding energies in the LVO/STO spectra, which is not present in the reference Nb:STO spectrum. This is known to originate from Ti³⁺ ions which host an additional electron in the 3d shell, leading to better screening of the core potential and hence a binding energy shift of the Ti 2p peaks to lower values [52]. As the spectral weight of the Ti³⁺ shoulder increases for higher emission angles θ (i.e. for higher interface sensitivity), these Ti³⁺ ions reside mainly at the interface.

Apart from the Ti³⁺ signal on the lower binding energy side, there is also a less pronounced broadening towards higher binding energies. Such a broadening can be even more clearly seen at the Sr 3d_{5/2} line, where one can also notice (see the red arrow) that the asymmetry becomes stronger towards higher electron emission angles, i.e., higher interface sensitivity. These asymmetries of core lines are ascribed to band bending, namely in the substrate towards the interface [51, 53]. The binding energies of all substrate core levels follow the corresponding electronic potential profile. Each layer in the substrate bending zone contributes a photoemission spectrum that is shifted with respect to the bulk, with the total spectrum being a superposition of all these contributions, resulting in a broadened and asymmetric peak shape. Here, apparently a downward band bending towards the interface is observed as with increasing interface sensitivity the spectra originating from closer to the interface exhibit a shift to higher binding energies.

To obtain quantitative estimates of the band bending, we introduce a model similar to Schütz *et al.* [53]. A visualization thereof is depicted in Fig. 9. We assume a potential profile of the form $E_{bb}(z) = \Delta E_{bb}(\frac{z}{d} - 1)^2$ for $0 < z < d$ and $E_{bb}(z) = 0$ elsewhere, with $E_{bb}(z)$ being the electrostatic potential at position z below the interface, ΔE_{bb} the energetic depth of the band bending and d the spatial extension of the bending zone. The photoemission signal from each layer of the substrate at depth z is assumed to be a symmetric Voigt peak with its energy position shifted by $E_{bb}(z)$. The intensity from each layer is damped according to equation (1). Note that the number of layers in the bending zone is not predetermined but a result of the fit. The contributions of all layers below the bending zone are summed up to constitute a single bulk peak. To improve the statistical reliability of our analysis we fit simultaneously with this model the five Sr 3d spectra and the five Ti 2p_{3/2} spectra collected at emission angles of 15°, 25°, 35°, 45°, and 55°. By this global fit we obtain the values of ΔE_{bb} and d with a total of 28 fitting parameters [54]. Figure 10 exemplifies the fitting results for the 6 uc LVO/STO sample. In general,

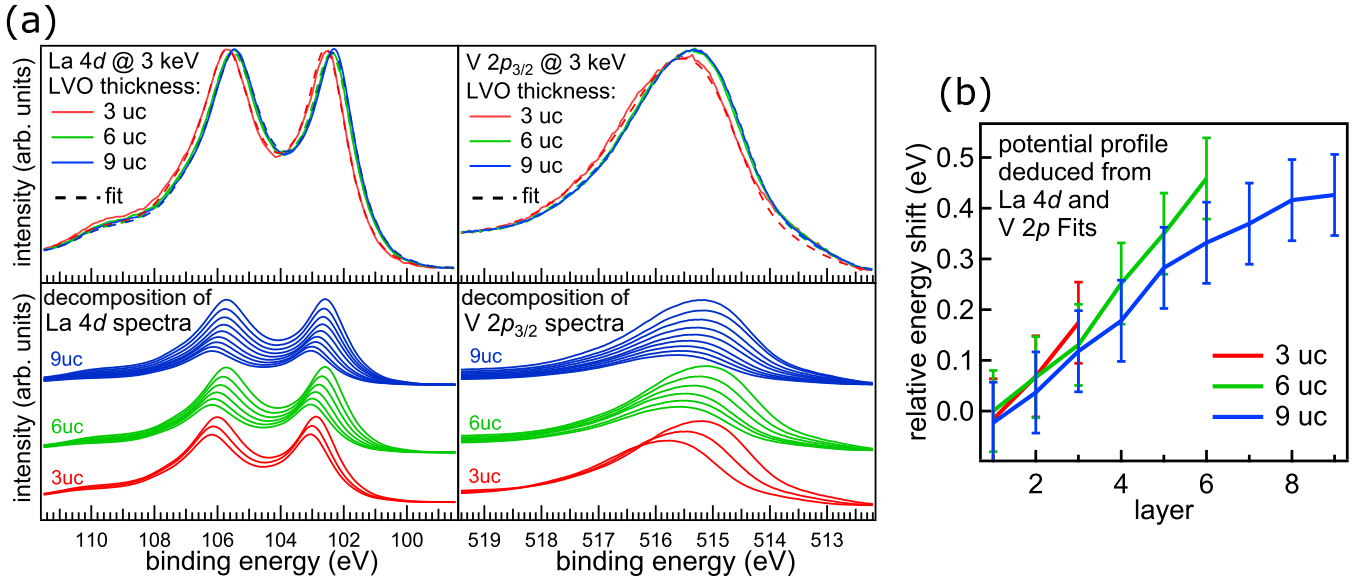


FIG. 7. (a) top: La 4d and V 2p_{3/2} spectra for three different LVO/STO samples with LVO film thicknesses of 3, 6 and 9 uc along with the corresponding fit curves. For both core levels, one can see an energy shift towards lower binding energies with increasing film thickness. The fits match the measured spectra fairly well. (a) bottom: Decomposition of the La 4d and V 2p fit curves into their single spectra for all three thicknesses. Each single spectrum is exponentially damped according to the depth of its corresponding layer while the energy position is determined by the fitting routine. (b) The potential profiles for each film as deduced from the fitting of the La 4d and V 2p spectra in (a). The energy shift of the first layer of the 6 uc sample at the interface (layer 1) is set to zero, with a positive shift indicating a shift to a lower binding energy.

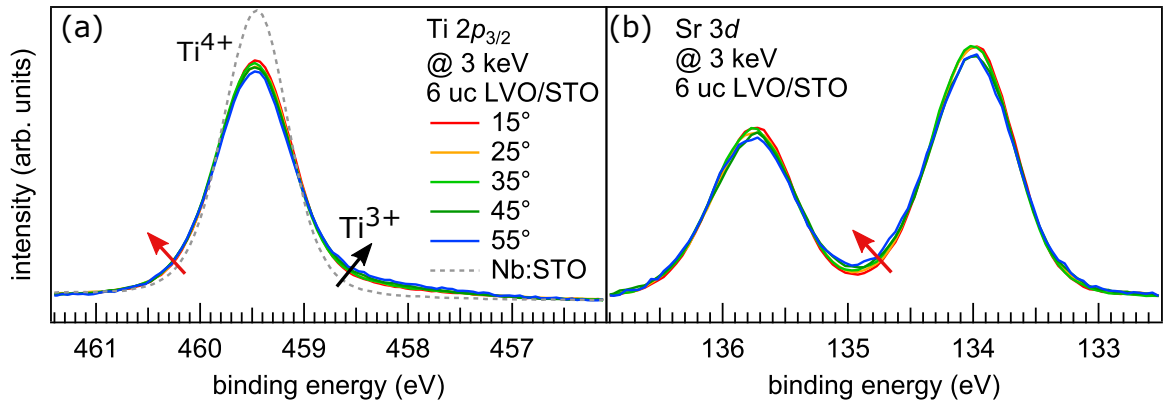


FIG. 8. Ti 2p_{3/2} (a) and Sr 3d (b) spectra of a 6 uc LVO/STO sample for different electron emission angles along with a Ti 2p_{3/2} reference spectrum of a Nb-doped STO substrate. Beside additional Ti³⁺ spectral weight at lower binding energies (black arrow), both core level lines show an asymmetry towards higher binding energies as well (red arrows).

the measured spectra are well reproduced by our model with negligible deviations supporting band bending being the main cause of the asymmetric peak shapes. Our quantitative analysis yields a value of 1.5 nm for the spatial extension of the bending zone d and about 0.4 eV for the energetic depth of the band bending ΔE_{bb} .

The fits in Fig. 10 (a) also confirm that the Ti³⁺ contribution rises for higher angles, reflecting the fact that Ti³⁺ ions reside at the interface.

C. Band offset between substrate and film from valence band analysis

A simple, accurate way to determine the band offset between substrate and film can be accomplished by analyzing the HAXPES valence band spectrum of a heterostructure [51, 55], which is a weighted superposition of the valence band spectra of the film and substrate. The band offset corresponds to the energy difference between the leading edges of the valence band spectra of the film and substrate. To determine the band offset, we measured the reference valence band spectra from

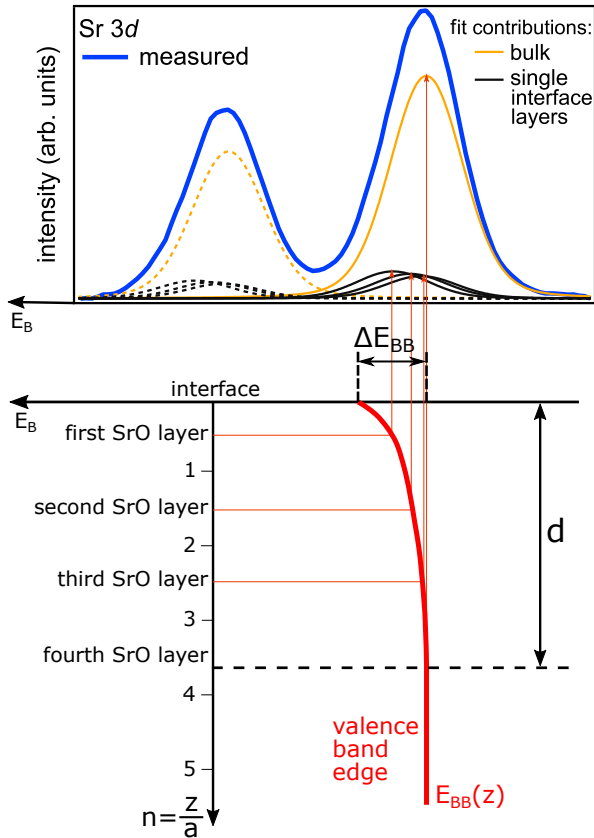


FIG. 9. Visualization of the interfacial band bending exemplified by a Sr 3d spectrum. The photoemission signal of each SrO layer at depth z is assumed to be a symmetric Voigt peak shifted in energy by $E_{bb}(z)$. The contributions from deeper layers without energy shift are treated as a single bulk peak. By assuming a quadratic potential within the bending zone, we can deduce the energetic depth of the band bending ΔE_{bb} and its spatial extension d .

an STO substrate and a thick (30 uc) LVO film, with which we fit the valence band spectrum of an LVO/STO heterostructure. The fitting parameters are the energy positions of the two spectra and their integral spectral weights. Figure 11 (a) depicts the valence band spectrum of a 6 uc LVO/STO sample and its decomposition into the LVO and STO contributions. For the fitting, we included the potential profile in the LVO film shown in Fig. 7 (b). Hence, the LVO contribution is composed of the six layer-resolved LVO valence band spectra that are shifted in binding energy according to this profile, which are depicted in Fig. 11 (b). The fitted spectrum is in very good agreement with the measured data. Note that there is a high contrast between the LVO and STO valence band spectra just below the Fermi energy where LVO shows spectral weight related to the lower Hubbard band whereas STO exhibits a gap. By comparing the binding energy difference between the valence band onsets of STO and LVO, which are determined by linear extrapolations of the leading edges to where zero intensity occurs, we obtain a valence band offset of about 0.3 eV.

However, since the LVO contribution is the sum of the single layers, the value for valence band onset, on which this analysis is based, is kind of averaged over the film. To derive a more precise value for the band offset at the interface, we compare the onsets of the valence band spectra of the bottom LVO layer [Fig. 11 (b)] and of the STO (bulk) contribution which yields 0. The onsets of the following layers track the potential gradient and hence shift to lower binding energies. The energy values depicted here are also derived from linear extrapolations of the leading edges. In particular, the valence band analysis allows us to complete our band scheme: The onset of the LHB of the top LVO layer is 0.15 eV below the Fermi energy. With an energy difference of 0.45 eV between the spectra of the bottom and top LVO layers, the onset of the LHB of the bottom layer is hence 0.6 eV below E_F .

We note that due to the large inelastic mean free path compared to the bending zone extension in STO the contribution of bulk STO to the valence band spectrum by far outweighs that of the bending zone. In addition, in the bending region the spectral onsets of the layer-resolved signals shift downwards. Consequently, the band bending in STO can be ignored in determining the valence band edge of STO.

D. Complete band diagram and summarizing discussion

Having determined the potential profile in LVO, the band bending of STO near the interface and the interfacial band offset, and referring to the reported optical gap of LVO of 1.1 eV [13, 14], we are able to derive the full electronic band diagram of the 6 uc LVO/STO heterostructure, as drawn in Fig. 12.

In a region extending from the interface into the substrate by about 1.5 nm, the Ti 3d conduction bands are bent downwards below the Fermi energy when approaching the interface. These states are filled by electrons, giving rise to a 2DES. The VB maxima of bulk STO and the first LVO layer at the interface are aligned, yielding a zero interfacial band offset. In the LVO film, there is a built-in potential due to the polar discontinuity which, however, is not large enough to shift the lowest lying excitations of the LHB up to the Fermi energy. The upper Hubbard band, in turn, lies way above the Fermi energy. Thus, no doping of V 3d-derived states takes place.

Our transport and photoemission experiments conclusively show that the conductivity in LVO/STO heterostructures above a critical thickness of 5 uc is generated by the intrinsic mechanism of electronic reconstruction, with Ti 3d interface states hosting mobile electrons. Self-doping within the LVO film can be excluded from the experimentally derived band diagram as well as vanadium core level spectra and ResPES measurements of the valence band, showing no indication for a change of the vanadium valence state throughout the film and V 3d spectral weight at E_F , respectively. Hence, a band-

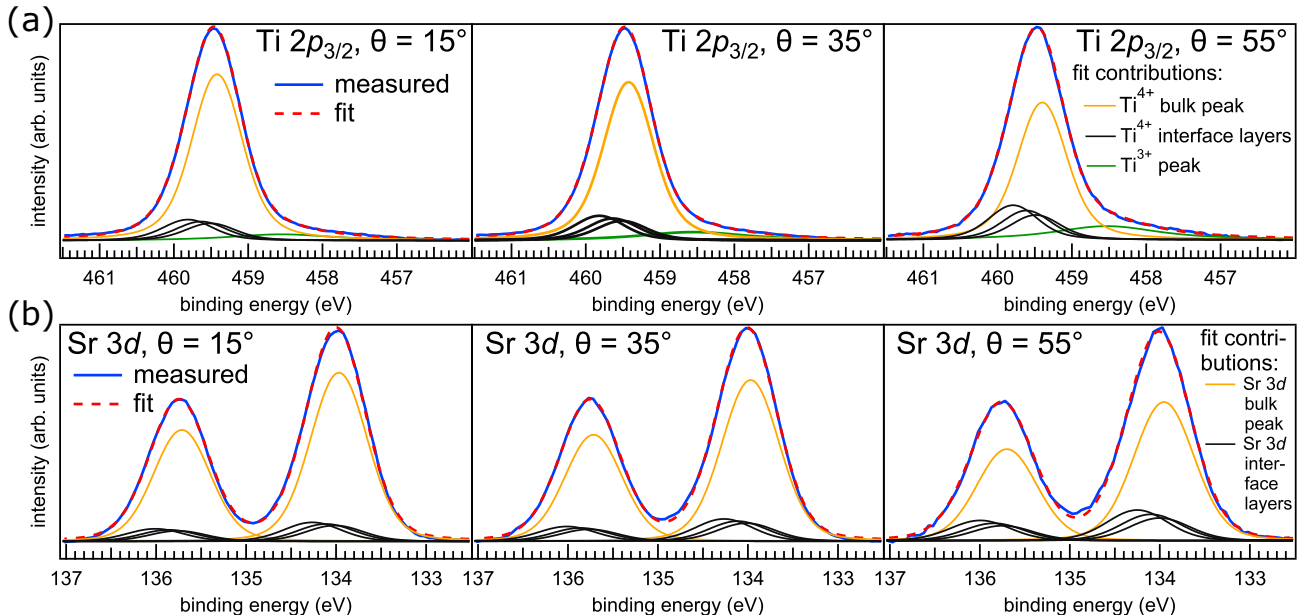


FIG. 10. (a) Exemplary fits for the Ti $2p_{3/2}$ photoemission spectra. The asymmetric line shape can be modeled by several, energetically shifted Voigt peaks, representing the individual layers in the bending zone, in addition to the Ti^{4+} bulk peak. Beside the dominant Ti^{4+} peak, there is an additional Ti^{3+} contribution. (b) Exemplary fits for the Sr $3d$ photoemission spectra. For each layer in the bending zone an energetically shifted spectrum is taken into account in addition to a single peak, representing the bulk contribution.

filling induced Mott-insulator-to-metal transition in LVO can be ruled out.

We find that the built-in potential is much lower than what is expected in the ideal picture of electronic reconstruction, based on density-functional calculations. Furthermore, the built-in potential does not cause a Fermi level crossing of occupied bands, in particular the LHB, in the film with increasing thickness. These observations can be reconciled in a refined picture of electronic reconstruction, as has been suggested for LAO/STO [44]. In this scenario, the interfacial charges do not stem from bands crossing the Fermi level but from defect states, in particular oxygen vacancies at the very film surface [26, 28, 57–59]. Although it costs energy to build these defects, at the critical thickness, the energy gain by transferring the released charges to the interface and thus partially compensating the polarization field predominates. Hence, for the system studied here, we suggest surface oxygen defects as charge reservoir for the interface 2DES.

Knowledge of the complete band diagram as derived in this study can be very useful for developing novel concepts for photovoltaic devices. Particularly, the advantages of the intrinsic electric field in LVO/STO can be combined with the benefits of the optical gap of LVO, which is in the ideal range for absorption of visible light. The measured potential gradient in the LVO film could help to separate photogenerated carriers without the need of creating a pn -junction by means of chemical doping. In addition, the induced metallic interface reported here can be used as a contact for extracting these carriers. As we find a sizable gradient only for

the first few layers and a gradient saturation for thicker films, one could think of LVO/STO superlattices with optimized LVO layer thicknesses just at or slightly above the critical value to maximize the potential build-up and facilitate the charge carrier separation. With suitable contacts on the metallic STO layers for optimized multiple carrier extraction, the photovoltaic property of the whole system can be greatly enhanced. Furthermore, it has been proposed to combine the LVO film with another material with a band gap in the solar range, e.g. LVO and LaFeO_3 [8]. With such band-gap graded designs the solar absorption can be increased even more by improving the conversion efficiency in the energy regions of the respective band gaps [60, 61]. The materials combination of LVO and STO (possibly combined with additional solar absorbing materials) may hence allow the superior properties of Mott materials, in terms of quantum efficiency and energy conversion, to be exploited for photovoltaic applications.

V. SUMMARY

Based on electrical transport and photoemission experiments we elucidate the mechanism leading to conductivity in the $\text{LaVO}_3/\text{SrTiO}_3$ heterostructure and the nature of the charge carriers. We find a critical film thickness of 5 uc for the onset of metallicity. The comparably low charge carrier concentration of less than 10^{14} cm^{-2} and the fact that its temperature dependence is almost

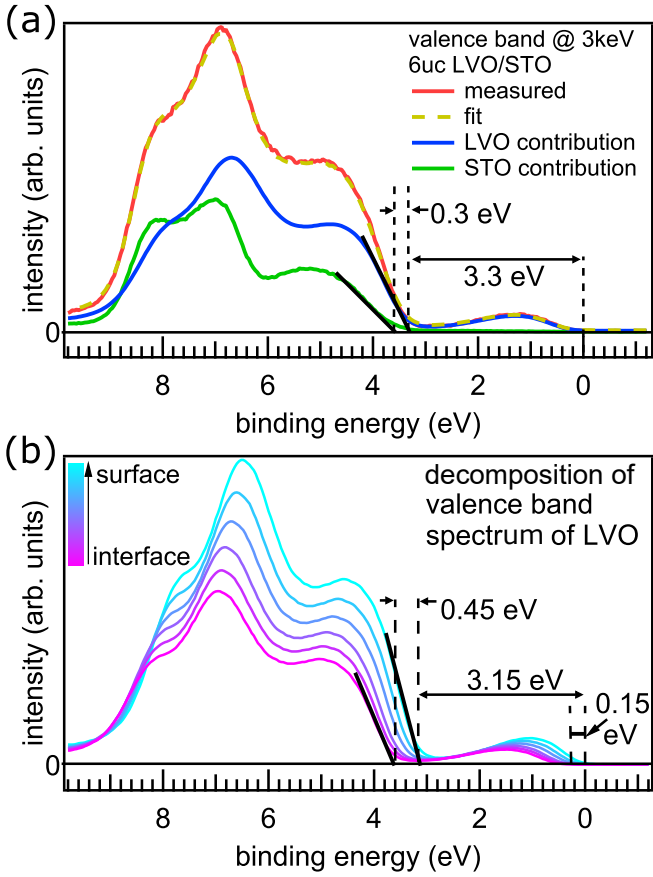


FIG. 11. (a) Valence band spectrum of a 6 uc LVO/STO heterostructure and its decomposition into the individual LVO and STO contributions. The valence band onsets are defined by linear extrapolations of the leading edges. (b) Layer-resolved decomposition of the LVO contribution from (a). The individual spectra are shifted in energy according to the potential profile.

identical to that of post-annealed $\text{LaAlO}_3/\text{SrTiO}_3$ leads us to the conclusion that conductivity is not induced by oxygen vacancies in the substrate but intrinsic in nature, viz., due to electronic reconstruction as a consequence of the polar discontinuity at the interface. From the photoemission spectra we infer a potential gradient in the LVO film of around 0.1 eV/uc for films up to 6 uc and a saturating behavior for larger thicknesses. In the substrate we find a downwards band bending with a spatial extension of about 1.5 nm and an energetic depth of about 0.4 eV . The conducting electrons reside in interfacial $\text{Ti } 3d$ states whereas no indications are found for occupied $\text{V } 3d$ states. We suggest surface oxygen vacancies as charge reservoir for the conducting interface.

The complete band diagram as derived from hard X-ray photoemission spectroscopy in combination with resistivity and Hall effect data in this study promote a better understanding of the $\text{LaVO}_3/\text{SrTiO}_3$ heterostructure. In particular, our results can help to harness the peculiar properties of Mott materials for tailored photovoltaic

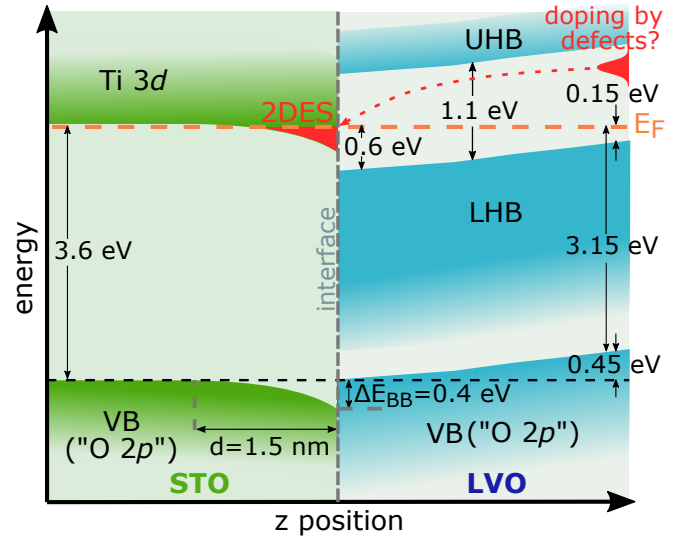


FIG. 12. Band diagram of the 6 uc LVO/STO heterostructure as deduced from core level and valence band photoemission, with the value of the optical gap - as defined by the energy difference between the onsets of lower (LHB) and upper Hubbard bands (UHB) - taken from literature. In the substrate, the bands are bending downwards towards the interface while there is an increasing potential slope in the film. The $\text{Ti } 3d$ bands, crossing the Fermi level, provide a pocket for electrons to form a two-dimensional electron system (2DES) at the interface. The LHB of the LVO film does not quite reach the Fermi level at the film surface. The bulk valence band offset is zero, since the valence band states of LVO and bulk STO, denoted by $\text{VB}(\text{"O } 2p\text{"})^a$, are aligned.

^a We note that for the energy regime of HAXPES, this part of the valence band contains contributions not only from oxygen but also to a significant amount from the A and B cations in film and substrate [56].

applications in future devices.

ACKNOWLEDGMENTS

The authors thank G. Sangiovanni for helpful discussions. The authors are grateful for funding support from the Deutsche Forschungsgemeinschaft (DFG, German Research Foundation) under Research grant SI 851/2-1 (Project ID 431448015) and through the Würzburg-Dresden Cluster of Excellence on Complexity and Topology in Quantum Matter ct.qmat (EXC 2147, Project ID 390858490) as well as through the Collaborative Research Center SFB 1170 ToCoTronics (Project ID 258499086). The authors acknowledge Diamond Light Source for time on beamline I09 under proposals SI17499 and SI23737. The authors would also like to thank D. McCue for technical support at beamline I09.

- [1] E. Morosan, D. Natelson, A. H. Nevidomskyy, and Q. Si, *Advanced Materials* **24**, 4896 (2012).
- [2] M. Uehara, S. Mori, C. H. Chen, and S.-W. Cheong, *Nature* **399**, 560 (1999).
- [3] H. Takagi and H. Y. Hwang, *Science* **327**, 1601 (2010).
- [4] C. H. Ahn, J.-M. Triscone, and J. Mannhart, *Nature* **424**, 1015 (2003).
- [5] T. Yajima, Y. Hikita, and H. Y. Hwang, *Nature materials* **10**, 198 (2011).
- [6] P. Scheiderer, M. Schmitt, J. Gabel, M. Zapf, M. Stübinger, P. Schütz, L. Dudy, C. Schlueter, T.-L. Lee, M. Sing, and R. Claessen, *Advanced Materials* **30**, 1706708 (2018).
- [7] A. Fujimori, T. Yoshida, K. Okazaki, T. Tsujioka, K. Kobayashi, T. Mizokawa, M. Onoda, T. Katsufuji, Y. Taguchi, and Y. Tokura, *Journal of Electron Spectroscopy and Related Phenomena Strongly correlated systems*, **117-118**, 277 (2001).
- [8] E. Assmann, P. Blaha, R. Laskowski, K. Held, S. Okamoto, and G. Sangiovanni, *Phys. Rev. Lett.* **110**, 078701 (2013).
- [9] H.-T. Zhang, M. Brahlek, X. Ji, S. Lei, J. Lapano, J. W. Freeland, V. Gopalan, and R. Engel-Herbert, *ACS Appl. Mater. Interfaces* **9**, 12556 (2017).
- [10] P. Werner, K. Held, and M. Eckstein, *Phys. Rev. B* **90**, 235102 (2014).
- [11] E. Manousakis, *Phys. Rev. B* **82**, 125109 (2010).
- [12] M. Eckstein and P. Werner, *Phys. Rev. Lett.* **113**, 076405 (2014).
- [13] L. Wang, Y. Li, A. Bera, C. Ma, F. Jin, K. Yuan, W. Yin, A. David, W. Chen, W. Wu, W. Prellier, S. Wei, and T. Wu, *Phys. Rev. Applied* **3**, 064015 (2015).
- [14] T. Arima, Y. Tokura, and J. B. Torrance, *Phys. Rev. B* **48**, 17006 (1993).
- [15] Y. Hotta, T. Susaki, and H. Y. Hwang, *Phys. Rev. Lett.* **99**, 236805 (2007).
- [16] M. Jellite, J. L. Rehspringer, M. A. Fazio, D. Muller, G. Schmerber, G. Ferblantier, S. Colis, A. Dinia, M. Sugiyama, A. Slaoui, D. Cavalcoli, and T. Fix, *Solar Energy* **162**, 1 (2018).
- [17] S. Goyal, A. Singh, R. Tomar, R. Kaur, C. Bera, and S. Chakraverty, *Solid State Communications* **316-317**, 113930 (2020).
- [18] G. Koster, B. L. Kropman, G. J. H. M. Rijnders, D. H. A. Blank, and H. Rogalla, *Appl. Phys. Lett.* **73**, 2920 (1998).
- [19] N. Nakagawa, H. Y. Hwang, and D. A. Muller, *Nature Materials* **5**, 204 (2006).
- [20] Z. Q. Liu, C. J. Li, W. M. Lü, X. H. Huang, Z. Huang, S. W. Zeng, X. P. Qiu, L. S. Huang, A. Annadi, J. S. Chen, J. M. D. Coey, T. Venkatesan, and Ariando, *Phys. Rev. X* **3**, 021010 (2013).
- [21] S. Thiel, G. Hammerl, A. Schmehl, C. W. Schneider, and J. Mannhart, *Science* **313**, 1942 (2006).
- [22] M. Takizawa, Y. Hotta, T. Susaki, Y. Ishida, H. Wadati, Y. Takata, K. Horiba, M. Matsunami, S. Shin, M. Yabashi, K. Tamasaku, Y. Nishino, T. Ishikawa, A. Fujimori, and H. Y. Hwang, *Phys. Rev. Lett.* **102**, 236401 (2009).
- [23] P. R. Willmott, S. A. Pauli, R. Herger, C. M. Schlepütz, D. Martoccia, B. D. Patterson, B. Delley, R. Clarke, D. Kumah, C. Cionca, and Y. Yacoby, *Phys. Rev. Lett.* **99**, 155502 (2007).
- [24] L. Qiao, T. C. Droubay, T. Varga, M. E. Bowden, V. Shutthanandan, Z. Zhu, T. C. Kaspar, and S. A. Chambers, *Phys. Rev. B* **83**, 085408 (2011).
- [25] G. Herranz, M. BasletiĆ, M. Bibes, C. Carrétéro, E. Tafr, E. Jacquet, K. Bouzehouane, C. Deranlot, A. Hamzić, J.-M. Broto, A. Barthélémy, and A. Fert, *Phys. Rev. Lett.* **98**, 216803 (2007).
- [26] Z. Zhong, P. X. Xu, and P. J. Kelly, *Phys. Rev. B* **82**, 165127 (2010).
- [27] Y. Xie, Y. Hikita, C. Bell, and H. Y. Hwang, *Nature communications* **2**, 494 (2011).
- [28] N. C. Bristowe, P. B. Littlewood, and E. Artacho, *Phys. Rev. B* **83**, 205405 (2011).
- [29] P. Scheiderer, F. Pfaff, J. Gabel, M. Kamp, M. Sing, and R. Claessen, *Phys. Rev. B* **92**, 195422 (2015).
- [30] L. Hu, R. H. Wei, X. W. Tang, S. J. Zhu, X. K. Zhang, X. B. Zhu, W. H. Song, J. M. Dai, C. J. Zhang, and Y. P. Sun, *Journal of Applied Physics* **125**, 145302 (2019).
- [31] H. Rotella, O. Copie, A. Pautrat, P. Boullay, A. David, D. Pelloquin, C. Labbé, C. Frilay, and W. Prellier, *J. Phys.: Condens. Matter* **27**, 095603 (2015).
- [32] A. Kalabukhov, R. Gunnarsson, J. Börjesson, E. Olsson, T. Claeson, and D. Winkler, *Phys. Rev. B* **75**, 121404 (2007).
- [33] A. F. Santander-Syro, O. Copie, T. Kondo, F. Fortuna, S. Pailhes, R. Weht, X. G. Qiu, F. Bertran, A. Nicolaou, A. Taleb-Ibrahimi, P. Le Fevre, G. Herranz, M. Bibes, N. Reyren, Y. Apertet, P. Lecoeur, A. Barthélémy, and M. J. Rozenberg, *Nature* **469**, 189 (2011).
- [34] W. Meevasana, P. D. C. King, R. H. He, S.-K. Mo, M. Hashimoto, A. Tamai, P. Songsiririthigul, F. Baumberger, and Z.-X. Shen, *Nature Materials* **10**, 114 (2011).
- [35] T. Rödel, C. Bareille, F. Fortuna, C. Baumier, F. Bertran, P. Le Fevre, M. Gabay, O. Hijano Cubelos, M. Rozenberg, T. Maroutian, P. Lecoeur, and A. Santander-Syro, *Phys. Rev. Applied* **1**, 051002 (2014).
- [36] S. McKeownWalker, A. de la Torre, F. Bruno, A. Tamai, T. Kim, M. Hoesch, M. Shi, M. Bahramy, P. King, and F. Baumberger, *Phys. Rev. Lett.* **113**, 177601 (2014).
- [37] S. M. Walker, F. Y. Bruno, Z. Wang, A. d. l. Torre, S. RiccÓ, A. Tamai, T. K. Kim, M. Hoesch, M. Shi, M. S. Bahramy, P. D. C. King, and F. Baumberger, *Advanced Materials* **27**, 3894 (2015).
- [38] L. Dudy, M. Sing, P. Scheiderer, J. D. Denlinger, P. Schütz, J. Gabel, M. Buchwald, C. Schlueter, T.-L. Lee, and R. Claessen, *Advanced Materials* **28**, 7443 (2016).
- [39] Y. Aiura, I. Hase, H. Bando, T. Yasue, T. Saitoh, and D. S. Dessau, *Surface Science* **515**, 61 (2002).
- [40] Z. Wang, Z. Zhong, X. Hao, S. Gerhold, B. Stöger, M. Schmid, J. Sánchez-Barriga, A. Varykhalov, C. Franchini, K. Held, and U. Diebold, *PNAS* **111**, 3933 (2014).
- [41] C. He, T. D. Sanders, M. T. Gray, F. J. Wong, V. V. Mehta, and Y. Suzuki, *Phys. Rev. B* **86**, 081401 (2012).
- [42] R. Tomar, R. M. Varma, N. Kumar, D. D. Sarma, D. Maryenko, and S. Chakraverty, *Advanced Materials Interfaces* **7**, 1900941 (2020).
- [43] J. Gabel, M. Zapf, P. Scheiderer, P. Schütz, L. Dudy, M. Stübinger, C. Schlueter, T.-L. Lee, M. Sing, and R. Claessen, *Phys. Rev. B* **95**, 195109 (2017).

- [44] G. Berner, M. Sing, H. Fujiwara, A. Yasui, Y. Saitoh, A. Yamasaki, Y. Nishitani, A. Sekiyama, N. Pavlenko, T. Kopp, C. Richter, J. Mannhart, S. Suga, and R. Claessen, *Phys. Rev. Lett.* **110**, 247601 (2013).
- [45] G. Drera, F. Banfi, F. F. Canova, P. Borghetti, L. Sangaletti, F. Bondino, E. Magnano, J. Huijben, M. Huijben, G. Rijnders, D. H. A. Blank, H. Hilgenkamp, and A. Brinkman, *Appl. Phys. Lett.* **98**, 052907 (2011).
- [46] H. Wadati, Y. Hotta, M. Takizawa, A. Fujimori, T. Susaki, and H. Y. Hwang, *Journal of Applied Physics* **102**, 053707 (2007).
- [47] E. Hryha, E. Rutqvist, and L. Nyborg, *Surface and Interface Analysis* **44**, 1022 (2012).
- [48] R. Zimmermann, R. Claessen, F. Reinert, P. Steiner, and S. Hüfner, *Journal of Physics: Condensed Matter* **10**, 5697 (1998).
- [49] S. A. Chambers, L. Qiao, T. C. Droubay, T. C. Kaspar, B. W. Arey, and P. V. Sushko, *Phys. Rev. Lett.* **107**, 206802 (2011).
- [50] R. Comes and S. Chambers, *Phys. Rev. Lett.* **117**, 226802 (2016).
- [51] G. Berner, A. Müller, F. Pfaff, J. Walde, C. Richter, J. Mannhart, S. Thiess, A. Gloskovskii, W. Drube, M. Sing, and R. Claessen, *Phys. Rev. B* **88**, 115111 (2013).
- [52] M. Sing, G. Berner, K. Goß, A. Müller, A. Ruff, A. Wetscherek, S. Thiel, J. Mannhart, S. A. Pauli, C. W. Schneider, P. R. Willmott, M. Gorgoi, F. Schäfers, and R. Claessen, *Phys. Rev. Lett.* **102**, 176805 (2009).
- [53] P. Schütz, F. Pfaff, P. Scheiderer, Y. Z. Chen, N. Pryds, M. Gorgoi, M. Sing, and R. Claessen, *Phys. Rev. B* **91**, 165118 (2015).
- [54] The number of parameters is narrowed down by physically reasonable constraints, e.g., each Sr $3d$ peak has the same Gaussian and the same Lorentzian full width at half maximum for every angle.
- [55] A. Giampietri, G. Drera, and L. Sangaletti, *Advanced Materials Interfaces* **4**, 1700144 (2017).
- [56] S. Thiess, T.-L. Lee, F. Bottin, and J. Zegenhagen, *Solid State Communications* **150**, 553 (2010).
- [57] Y. Li, S. N. Phattalung, S. Limpijumnong, J. Kim, and J. Yu, *Phys. Rev. B* **84**, 245307 (2011).
- [58] N. Pavlenko, T. Kopp, E. Y. Tsymbal, J. Mannhart, and G. A. Sawatzky, *Phys. Rev. B* **86**, 064431 (2012).
- [59] L. Yu and A. Zunger, *Nat Commun* **5**, 1 (2014).
- [60] G. Sassi, *Journal of Applied Physics* **54**, 5421 (1983).
- [61] M. Konagai and K. Takahashi, *Journal of Applied Physics* **46**, 3542 (1975).